Supporting Information

Strain-Modulated Interlayer Charge and Energy Transfers in MoS_2/WS_2 Heterobilayer

Joon-Seok Kim,[1,2,*] Nikhilesh Maity,[3] Myungsoo Kim,[2] Suyu Fu,[4] Rinkle Juneja,[3] Abhishek Singh,[3,*] Deji Akinwande,[2,*] and Jung-Fu Lin[4,*]

[1] Department of Materials Science and Engineering, Northwestern University, Evanston, IL 60208, USA

[2] Microelectronics Research Center, The University of Texas at Austin, Austin, TX 78758, USA

[3] Materials Research Centre, Indian Institute of Science, Bangalore 560012, India

[4] Department of Geological Sciences, Jackson School of Geosciences, The University of Texas at Austin, Austin TX 78712, USA

* joonseok.kim@northwestern.edu

* abhishek@mrc.iisc.ernet.in

* deji@ece.utexas.edu

* afu@jsg.utexas.edu

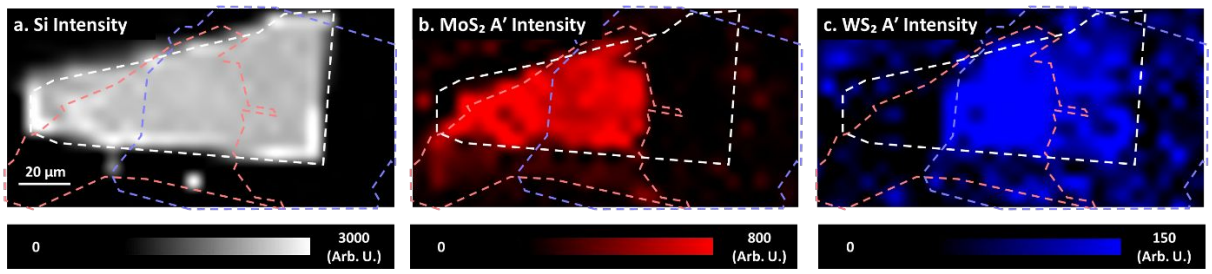

Figure S1. Raman intensity maps of the MoS_2/WS_2 heterostructure on Si chip, showing (a) Si peak, (b) MoS_2 A′ peak, and (c) WS_2 A′ peak intensities. The outlines of the Si/Al_2O_3 substrate, 1L-MoS_2, and 1L-WS_2 are indicated as white, red, and blue dotted lines, respectively.

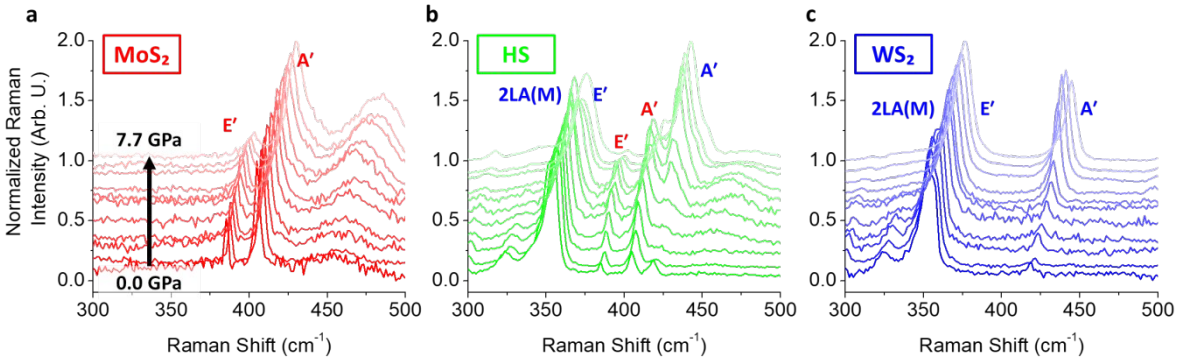

Figure S2. Evolution of Raman spectra of (a) 1L-MoS_2, (b) MoS_2/WS_2 heterostructure, and (c) 1L-WS_2 with increased pressure.

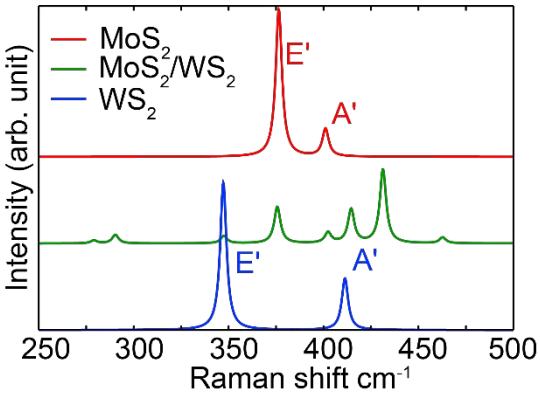

Figure S3. Calculated Raman active modes of the 1L-MoS_2, 1L-WS_2, and their heterostructure in ambient pressure conditions. Note that the calculated peak positions slightly deviate from experimental values, by a smaller margin compared to the literature.[1–3] The deviation may be attributed to the approximations used in the calculation, such as frozen phonon method, use of finite size supercell force constant, and vdW force approximation.

Note S1.

For the theoretical calculations of strain, the total energy costs due to the compressions have been calculated and shown in Figure S4. More specifically, the hydrostatic pressure has been modeled[4] by estimating the ease of compression along the x, y, and z direction: $\varepsilon_x = \frac{x - x_0}{x_0}$, $\varepsilon_y = \frac{y - y_0}{y_0}$, and $\varepsilon_z = \frac{z - z_0}{z_0}$, where ε_x, ε_y, and ε_z are the uniaxial strain along the x, y, and z directions, respectively. The weak vdW interaction along the z-direction results in low energy cost for the out-of-plane direction compared to the in-plane direction, therefore $\varepsilon_x = \varepsilon_y \neq \varepsilon_z$. In order to discriminate pressure in each axis, we investigated the individual energy cost for in-plane-only ($\varepsilon_x = \varepsilon_y \neq 0$; $\varepsilon_z = 0$) and out-of-plane-only ($\varepsilon_x = \varepsilon_y = 0$; $\varepsilon_z \neq 0$) components. The hydrostatic pressure was mimicked by estimating the compression in all directions based

on the total energy cost consumption (Figure S4). Consequently, applied effective pressure was determined using the the energy cost per unit volume change of the system by using the given equation,

$$P = \frac{E_0 - E}{V_0 - V} \quad (1)$$

where, E and E_0 are the total energy for the strained and unstrained systems, respectively, and V and V_0 are the volume of the strained and unstrained systems, respectively. The volume of the cell is defined as $V = a^2 c \sin(60)$, where a is the lattice parameter, and c is the thickness of the layer.[5]

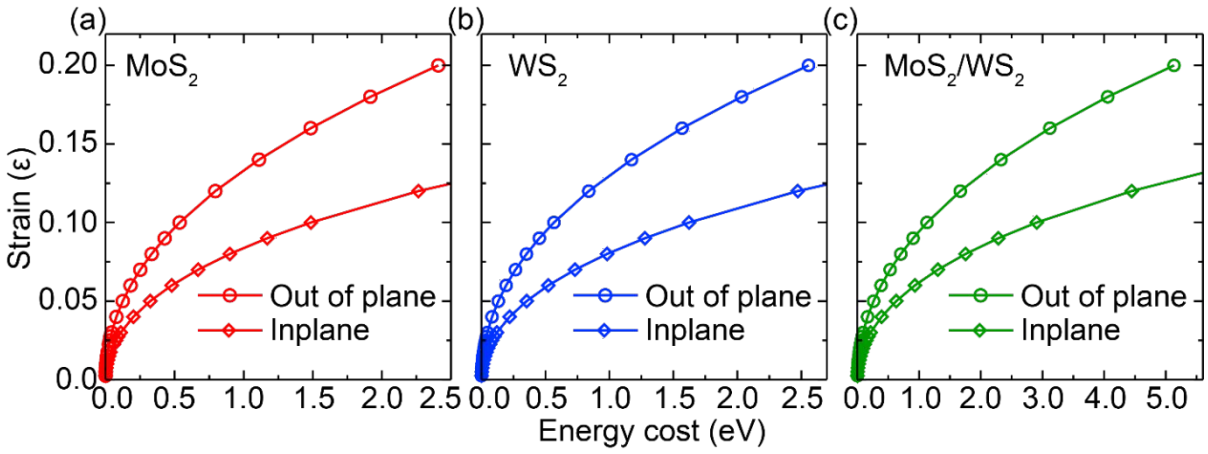

Figure S4. Modeling of hydrostatic pressure of the TMDCs monolayer. The variation of the applied strain with respect to the energy cost to compress the in-plane and out-of-plane bonds. (a) 1L-MoS_2 (b) 1L-WS_2, and (c) MoS_2/WS_2 heterostructure.

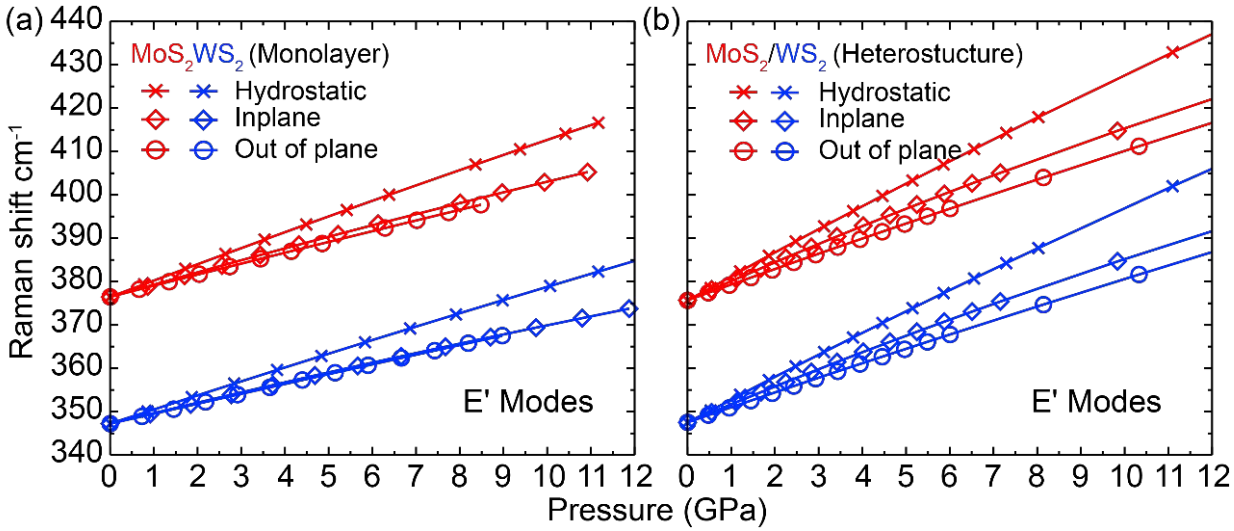

Figure S5. Calculated E′ mode frequencies under hydrostatic, in-plane, and out-of-plane stress components (a) for MoS_2 and WS_2 monolayers, and (b) for MoS_2/WS_2 heterobilayer.

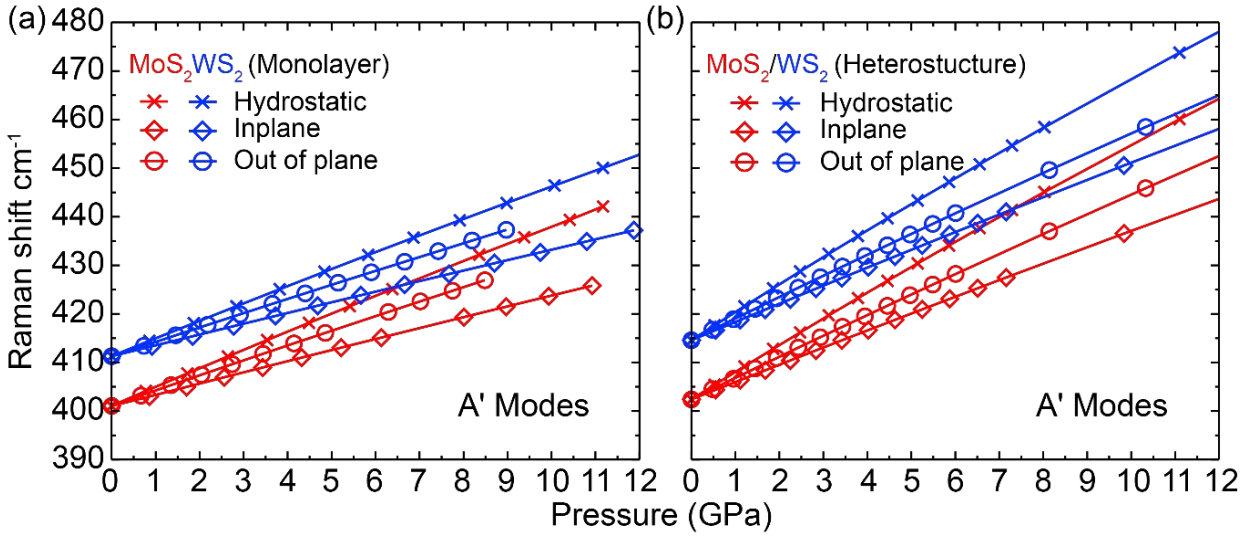

Figure S6. Calculated A′ mode frequencies under hydrostatic, in-plane, and out-of-plane stress components (a) for MoS_2 and WS_2 monolayers, and (b) for MoS_2/WS_2 heterobilayer.

$d\omega/dp$ (cm^{-1}/GPa)	Hydrostatic			In-plane			Out-of-plane		
	MoS_2	WS_2	MoS_2/ WS_2	MoS_2	WS_2	MoS_2/ WS_2	MoS_2	WS_2	MoS_2/ WS_2
E′ mode	3.60	3.13	4.96/ 4.73	2.64	2.23	3.74/ 3.56	2.50	2.26	3.41/ 3.27
A′ mode	3.66	3.45	4.99/ 5.11	2.27	2.18	3.41/ 3.59	3.04	2.90	4.18/ 4.21

Table S1. Summarized calculated blueshift rate of in-plane E′ and out-of-plane A′ modes with in-plane strain, out-of-plane strain, and hydrostatic pressure.

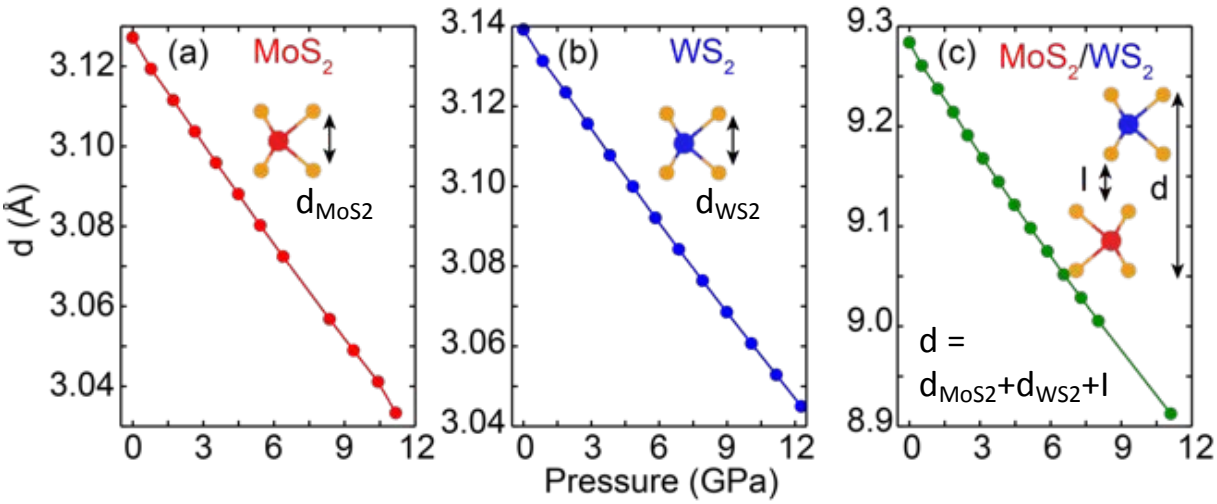

Figure S7. Calculated variation of intralayer S-S distance (d) with hydrostatic pressure for (a) monolayer MoS_2 and (b) monolayer WS_2. (c) The variation of total inter S-S distance of heterostructure, where the interlayer distance (I) is the most effectively reduced.

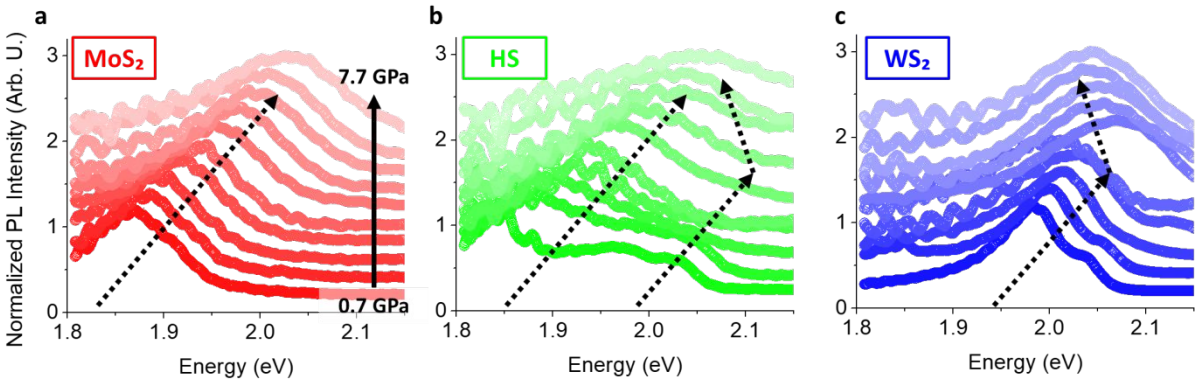

Figure S8. Evolution of PL spectra of (a) 1L-MoS_2, (b) MoS_2/WS_2 heterostructure, and (c) 1L-WS_2 with increased pressure. Dashed lines are a guide of PL peak energy changes.

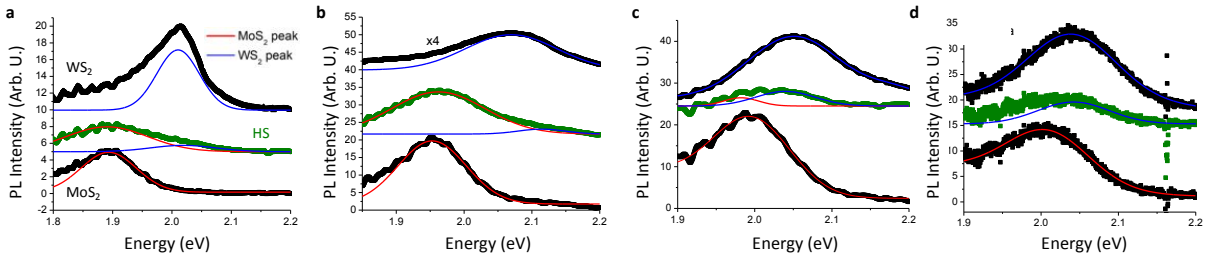

Figure S9. PL spectra of MoS_2-only (bottom), WS_2-only (top), and HS (middle) regions at representative pressures of (a) 2.1 GPa, (b) 4.1 GPa, (c) 5.8 GPa, and (d) 6.6 GPa. MoS_2-like and WS_2-like Gaussian lineshapes are shown in red and blue curves, respectively. At pressure 4.1 GPa and lower, WS_2-like PL signal is strongly quenched in the HS spectra, whereas at higher pressures, WS_2-like PL signal is less quenched in the HS spectra

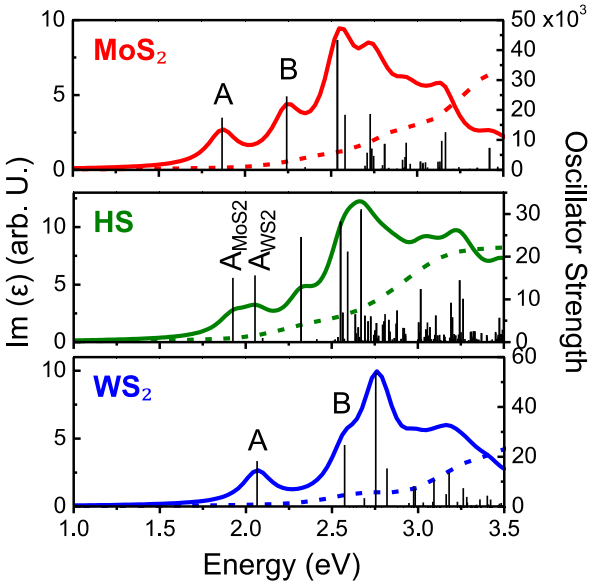

Figure S10. Optical absorption spectra of MoS_2/WS_2 heterostructure calculated by BSE (with e-h interaction; solid lines) and RPA (without e-h interaction; dotted lines) with A_{MoS2}, B_{MoS2}, A_{WS2} and B_{WS2} excitons. The vertical black lines represent the oscillator strength for the optical transition.

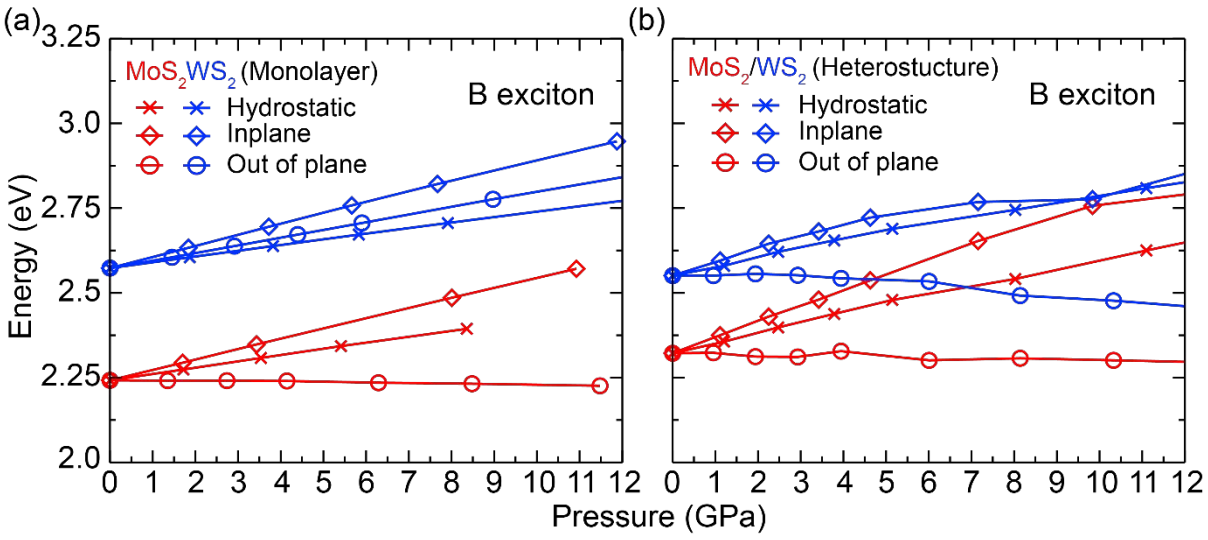

Figure S11. B Exciton energy levels as a function of hydrostatic pressure and corresponding in-plane and out-of-plane strain component (a) for MoS_2 and WS_2 monolayers, and (b) for MoS_2/WS_2 heterobilayer.

dE_g/dp (meV/GPa)	Hydrostatic			In-plane			Out-of-plane		
	MoS_2	WS_2	MoS_2/ WS_2	MoS_2	WS_2	MoS_2/ WS_2	MoS_2	WS_2	MoS_2/ WS_2
A exciton	12.69	12.11	17.63/ 13.47	32.63	34.19	49.85/ 55.22	-9.06	9.14	-13.06 /-21.58
B exciton	18.22	22.46	26.75/ 22.23	30.14	31.56	39.50/ 23.19	-1.44	16.55	-2.11 /-8.41

Table S2. Summarized the rate of variation of A and B excitonic energy levels with in-plane, out-of-plane, and hydrostatic pressure.

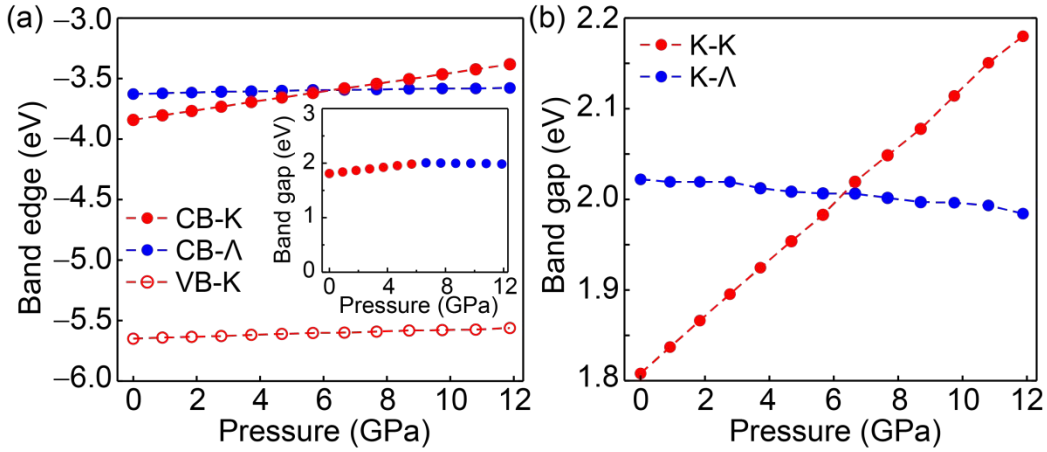

Figure S12. (a) Variation of conduction band (CB) edges at K and Λ and valence band (VB) edge at K as a function of in-plane pressure in WS_2. The inset indicates the variation of WS_2 band gap, where red and blue circles indicate direct and indirect band gap, respectively. (b) Closer view of the band gap variation, showing direct-to-indirect band gap transition of WS_2.

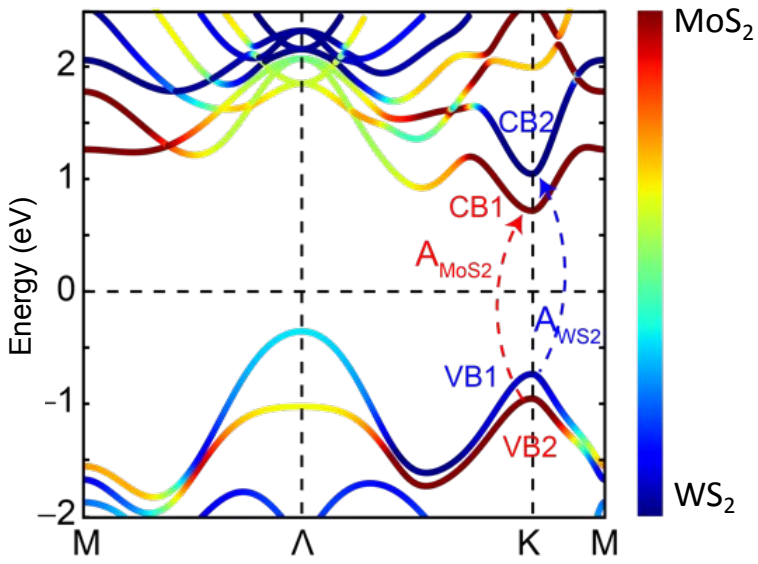

Figure S13. Hybridized band structure of MoS_2/WS_2 heterostructure in GGA-PBE approximation. The color gradient map indicates the projection of bands into isolated monolayers. Also, it is worth emphasizing that the Λ-K indirect bandgap is also clearly visible for WS_2-dominant (blue) bands.

Note S2. Estimation of Interlayer CT/ET Rates

PL intensity is closely governed by the excitonic lifetimes, namely

$$\frac{1}{\tau_E} = \frac{1}{\tau_R} + \frac{1}{\tau_{NR}} + \frac{1}{\tau_{IL}} \tag{2}$$

where τ_E, τ_R, τ_{NR}, and τ_{IL} correspond to exciton's total lifetime, radiative lifetime, non-radiative lifetime, and lifetime of interlayer charge/energy transfer in the case of heterostructure, respectively.[6] (In case of monolayers, $\tau_{IL} \rightarrow \infty$.) PL intensities of monolayer and heterostructure can then be expressed as

$$I_{mono} \propto \frac{\tau_E}{\tau_R} = \frac{\tau_{NR}}{\tau_R + \tau_{NR}} \tag{3}$$

and

$$I_{hetero} \propto \frac{\tau_E}{\tau_R} = \frac{\tau_{NR}\tau_{IL}}{\tau_{NR}\tau_{IL} + \tau_R\tau_{IL} + \tau_R\tau_{NR}} = \eta \times \frac{\tau_{NR}}{\tau_R + \tau_{NR}} \tag{4}$$

, respectively, with the introduction of the intensity ratio η. These equations take into account various non-radiative recombination pathways such as defect state-assisted recombination and scattering.

The τ_{IL} then can be expressed as

$$\tau_{IL} = \frac{\eta}{1-\eta} \times \frac{\tau_R\tau_{NR}}{\tau_R + \tau_{NR}}. \tag{5}$$

Assuming τ_{NR} ≈20 ps and τ_{NR} ≈200 ps for WS2,[7,8] the change in η from ≈0.3 at pressure below 1 GPa to ≈0.03 at 3-4 GPa corresponds to the τ_{IL} changing from ≈7.8 ps to ≈560 fs, more than an order of magnitude change. The enhancement factor reaching unity at 7.7 GPa implies significant reduction of interlayer transfer (Figure S12). We note that this estimation is in the similar order of magnitude with the timescale to form charge transfer equilibrium at band extrema.[9]

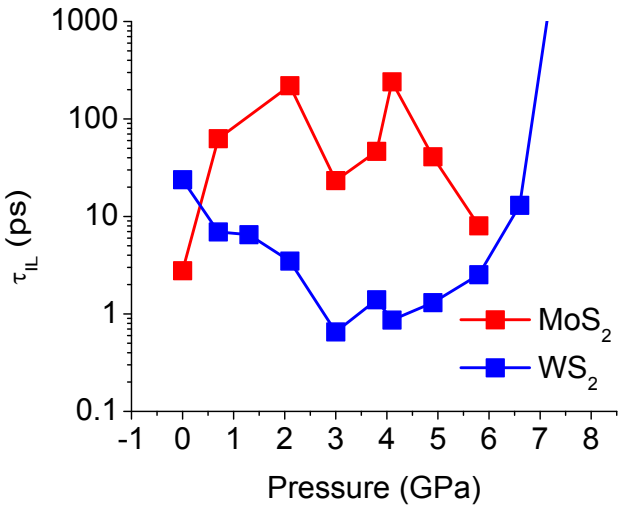

Figure S14. Estimated lifetime of interlayer charge/energy transfers.

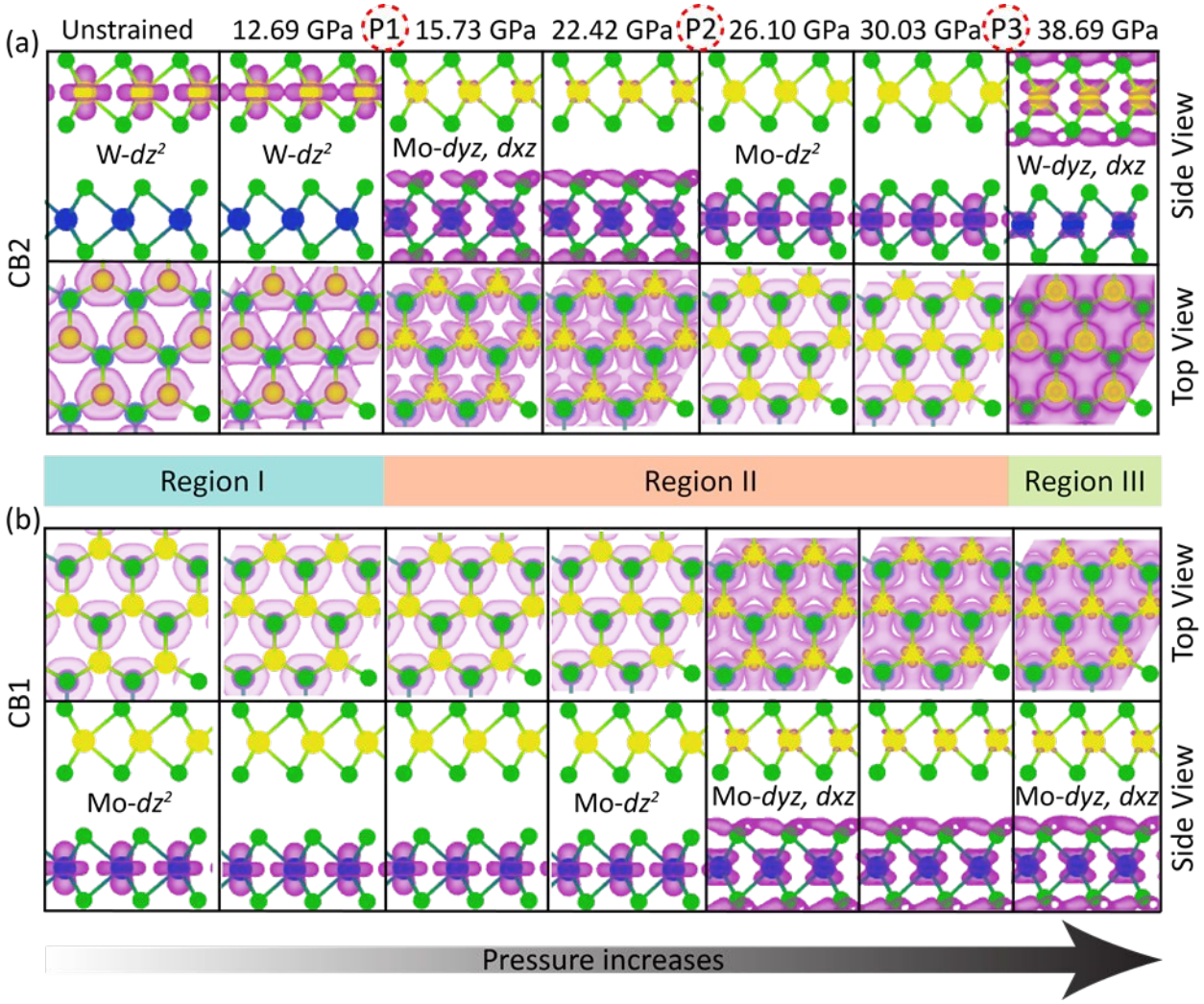

Figure S15. Band-decomposed charge densities of MoS_2/WS_2 heterostructure for (a) CB1 and (b) CB2, as viewed along the z-direction (Top View) and x-y plane (Side view). The top view of the CB1 and CB2 shows that shape of the charge distributions (dz^2 orbital) for the unstrained case is circular with smooth edges. With the application of strain, the shape of the charge distribution turns into a hexagonal shape with sharp edges. At the critical transition points, the charge distribution shape becomes completely hexagon, and the corner of each hexagon overlap with each other.

Note S3. Molecular Orbital Diagram

The valence bands and the frontier occupied bands (near the Fermi level) are antibonding in nature, whereas the remaining core valence bands have bonding nature. For unstrained monolayers, dxy and dx^2-y^2 are the highest occupied (VB1) antibonding orbitals of transition metal along with small contribution from p_x and p_y states of chalcogen atoms of the respective monolayers. While in MoS_2/WS_2 vdW heterostructure, they originate from W-dxy and dx^2-y^2 and minute contributions from S (WS_2)-p_x and p_y (Figure S13a). The lowest unoccupied (CB1) antibonding states are contributed by d_z^2 of transition metal and p_x, p_y of chalcogen atoms of the respective monolayers, while in MoS_2/WS_2, it originates from Mo-S, d_z^2 and S (MoS_2)-p_x, p_y orbitals (Figure S13a).

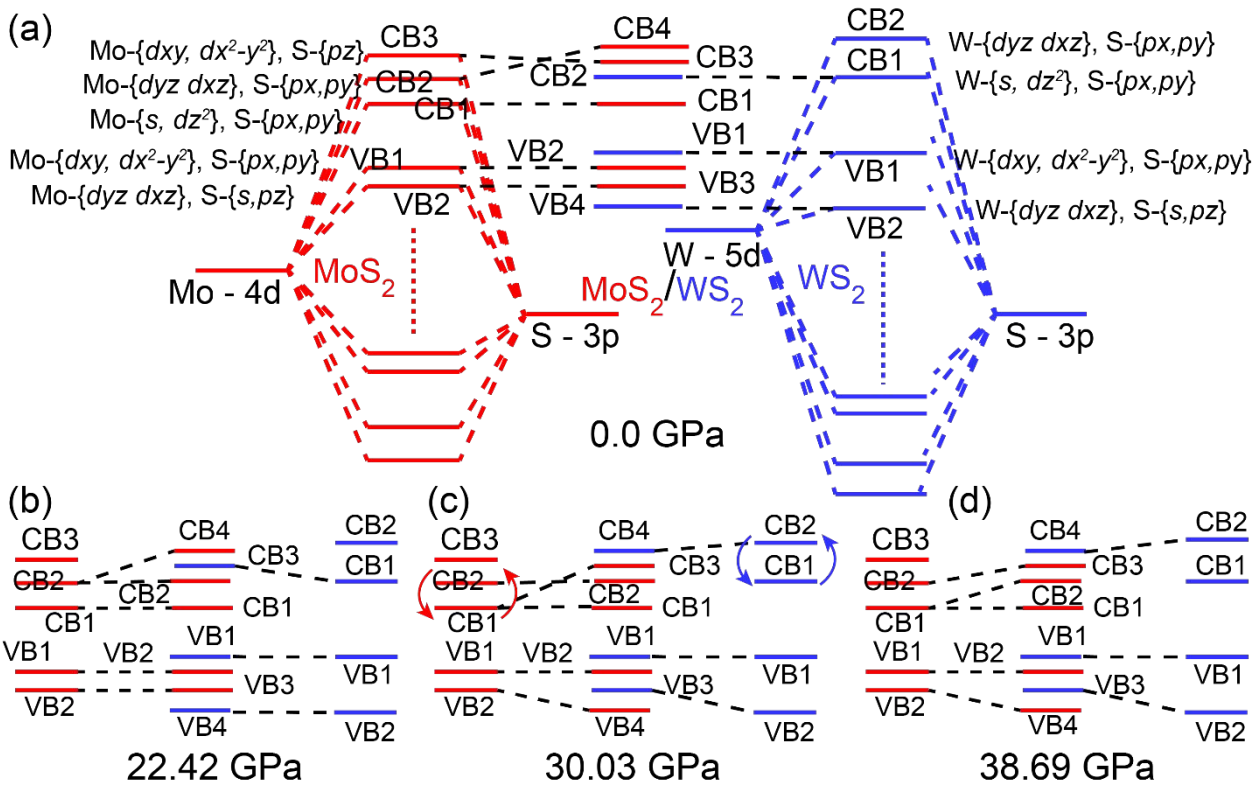

Figure S16. Molecular orbital (MO) diagram of monolayer MoS_2 (left; red), MoS_2/WS_2 vdW heterostructure (middle) and WS_2 (right; blue) at (a) unstrained condition, (b) at pressure between P1 and P2, (c) at pressure between P2 and P3, and (d) pressure above P3.

Bands	Unstrained (0%)	22.42 GPa (8%)	30.03 GPa (10%)	38.69 GPa (12%)
CB4	[Mo - *dxy*, dx^2] [$S(MoS_2)$ - *pz*]	[Mo - *dyz*, *dxz*] [$S(MoS_2)$ - *px*, *py*]	[W – *s*, dz^2] [$S(WS_2)$ - *px*, *py*]	[W – *s*, dz^2] [$S(WS_2)$ - *px*, *py*]
CB3	[Mo - *dyz*, *dxz*] [$S(MoS_2)$ - *px*, *py*]	[W – *s*, dz^2] [$S(WS_2)$ - *px*, *py*]	[Mo - *dyz*, *dxz*] [$S(MoS_2)$ - *px*, *py*]	[Mo - *s*, dz^2] [$S(MoS_2)$ - *px*, *py*]
CB2	[W – *s*, dz^2] [$S(WS_2)$ - *px*, *py*]	[Mo - *dyz*, *dxz*] [$S(MoS_2)$ - *px*, *py*]	[Mo - *s*, dz^2] [$S(MoS_2)$ - *px*, *py*]	[Mo - *dyz*, *dxz*] [$S(MoS_2)$ - *px*, *py*]
CB1	[Mo - *s*, dz^2] [$S(MoS_2)$ - *px*, *py*]	[Mo - *s*, dz^2] [$S(MoS_2)$ - *px*, *py*]	[Mo - *dyz*, *dxz*] [$S(MoS_2)$ - *px*, *py*]	[Mo - *dyz*, *dxz*] [$S(MoS_2)$ - *px*, *py*]
VB1	[W - *dxy*, dx^2] [$S(WS_2)$ - *px*, *py*]	[W – *dxy*, dx^2] [$S(WS_2)$ - *px*, *py*]	[W – *dxy*, dx^2] [$S(WS_2)$ - *px*, *py*]	[W – *dxy*, dx^2] [$S(WS_2)$ - *px*, *py*]
VB2	[Mo - *dxy*, dx^2] [$S(MoS_2)$ - *px*,*py*]	[Mo – *dxy*, dx^2] [$S(MoS_2)$ - *px*,*py*]	[Mo – *dxy*, dx^2] [$S(MoS_2)$ - *px*,*py*]	[Mo – *dxy*, dx^2] [$S(MoS_2)$ - *px*,*py*]
VB3	[Mo - *dyz*, *dxz*] [$S(MoS_2)$ - *s*, *pz*]	[Mo - *dyz*, *dxz*] [$S(MoS_2)$ - *s*, *pz*]	[W - *dyz*, *dxz*] [$S(WS_2)$ - *s*, *pz*]	[W - *dyz*, *dxz*] [$S(WS_2)$ - *s*, *pz*]
VB4	[W - *dyz*, *dxz*] [$S(WS_2)$ - *s*, *pz*]	[W - *dyz*, *dxz*] [$S(WS_2)$ - *s*, *pz*]	[Mo - *dyz*, *dxz*] [$S(MoS_2)$ - *s*, *pz*]	[Mo - *dyz*, *dxz*] [$S(MoS_2)$ - *s*, *pz*]

Table S3. The contribution of electronic states of frontier occupied and unoccupied bands at K point in stained and unstrained MoS_2/WS_2 vdW heterostructure. Red and blue arrows indicate changes in states in MoS_2 and WS_2, respectively, whereas black arrows indicate no changes.

Bands	Unstrained (0%)	22.42 GPa (8%)	30.03 GPa (10%)	38.69 GPa (12%)
CB4	[Mo - dyz, dxz] [S - pz, s]	[Mo - dyz, dxz] [S - pz, s]	[Mo - dyz, dxz] [S - pz, s]	[Mo - dyz, dxz] [S - pz, s]
CB3	[Mo - dx^2, dxy] [S - pz]	[Mo - dx^2, dxy] [S - pz]	[Mo - dx^2, dxy] [S - pz]	[Mo - dx^2, dxy] [S - pz]
CB2	[Mo - dyz, dxz] [S - px, py]	[Mo - dyz, dxz] [S - px, py]	[Mo - s, dz^2] [S - px, py]	[Mo - s, dz^2] [S - px, py]
CB1	[Mo - s, dz^2] [S - px, py]	[Mo - s, dz^2] [S - px, py]	[Mo - dyz, dxz] [S - px, py]	[Mo - dyz, dxz] [S - px, py]
VB1	[Mo - dxy, dx^2] [S - px, py]	[Mo - dxy, dx^2] [S - px, py]	[Mo - dxy, dx^2] [S - px, py]	[Mo - dxy, dx^2] [S - px, py]
VB2	[Mo - dyz, dxz] [S - s, pz]	[Mo - dyz, dxz] [S - s, pz]	[Mo - dyz, dxz] [S - s, pz]	[Mo - dyz, dxz] [S - s, pz]
VB3	[Mo - pz] [S - px, py]	[Mo - pz] [S - px, py]	[Mo - pz] [S - px, py]	[Mo - dxy, dx^2] [S - s, pz]
VB4	[Mo - dxy, dx^2] [S - s, pz]	[Mo - dxy, dx^2] [S - s, pz]	[Mo - dxy, dx^2] [S - s, pz]	[Mo - pz] [S - px, py]

Table S4. The contribution of electronic states in stained and unstrained MoS_2 monolayer in frontier occupied and unoccupied bands at K point. Red arrows indicate changes in states, whereas black arrows indicate no changes.

Bands	Unstrained (0%)	22.42 GPa (8%)	30.03 GPa (10%)	38.69 GPa (12%)
CB4	[W - dyz, dxz] [S - pz, s]	[W - dyz, dxz] [S - pz, s]	[W - dyz, dxz] [S - pz, s]	[W - dyz, dxz] [S - pz, s]
CB3	[W - dx^2, dxy] [S - pz]	[W - dx^2, dxy] [S - pz]	[W - dx^2, dxy] [S - pz]	[W - dx^2, dxy] [S - pz]
CB2	[W - dyz, dxz] [S - px, py]	[W - dyz, dxz] [S - px, py]	[W - s, dz^2] [S - px, py]	[W - s, dz^2] [S - px, py]
CB1	[W - s, dz^2] [S - px, py]	[W - s, dz^2] [S - px, py]	[W - dyz, dxz] [S - px, py]	[W - dyz, dxz] [S - px, py]
VB1	[W - dxy, dx^2] [S - px, py]	[W - dxy, dx^2] [S - px, py]	[W - dxy, dx^2] [S - px, py]	[W - dxy, dx^2] [S - px, py]
VB2	[W - dyz, dxz] [S - s, pz]	[W - dyz, dxz] [S - s, pz]	[W - dyz, dxz] [S - s, pz]	[W - dyz, dxz] [S - s, pz]
VB3	[W - pz] [S - px, py]	[W - pz] [S - px, py]	[W - pz] [S - px, py]	[W - dxy, dx^2] [S - s, pz]
VB4	[W - dxy, dx^2] [S - s, pz]	[W - dxy, dx^2] [S - s, pz]	[W - dxy, dx^2] [S - s, pz]	[W - pz] [S - px, py]

Table S5. The contribution of electronic states in stained and unstrained WS_2 monolayer in frontier occupied and unoccupied bands at K point. Blue arrows indicate changes in states, whereas black arrows indicate no changes.

REFERENCES

(1) Marmolejo-Tejada, J. M.; Fix, J. P.; Kung, P.; Borys, N. J.; Mosquera, M. A. Theoretical Analysis of the Nanoscale Composition, Tip-Enhanced Raman Spectroscopy, and Electronic Properties of Alloys in 2D MoS2–WS2 Heterostructures. *The Journal of Physical Chemistry C* **2022**, *126* (21), 9099–9108. https://doi.org/10.1021/ACS.JPCC.2C01535.

(2) McCreary, A.; Simpson, J. R.; Wang, Y.; Rhodes, D.; Fujisawa, K.; Balicas, L.; Dubey, M.; Crespi, V. H.; Terrones, M.; Hight Walker, A. R. Intricate Resonant Raman Response in Anisotropic ReS2. *Nano Letters* **2017**, *17* (10), 5897–5907. https://doi.org/10.1021/ACS.NANOLETT.7B01463

(3) Zhou, Y.; Maity, N.; Rai, A.; Juneja, R.; Meng, X.; Roy, A.; Zhang, Y.; Xu, X.; Lin, J.-F.; Banerjee, S. K.; Singh, A. K.; Wang, Y.; Zhou, Y.; Meng, X.; Wang, Y.; Maity, N.; Juneja, R.; Singh, A. K.; Rai, A.; Roy, A.; Banerjee, S. K.; Zhang, Y.; Lin, J.; Xu, X. Stacking-Order-Driven Optical Properties and Carrier Dynamics in ReS2. *Advanced Materials* **2020**, *32* (22), 1908311. https://doi.org/10.1002/ADMA.201908311.

(4) Nayak, A. P.; Pandey, T.; Voiry, D.; Liu, J.; Moran, S. T.; Sharma, A.; Tan, C.; Chen, C.; Li, L.-J.; Chhowalla, M.; Lin, J.-F.; Singh, A. K.; Akinwande, D. Pressure-Dependent Optical and Vibrational Properties of Monolayer Molybdenum Disulfide. *Nano Letters* **2015**, *15* (1), 346–353. https://doi.org/10.1021/nl5036397.

(5) Nayak, A. P.; Bhattacharyya, S.; Zhu, J.; Liu, J.; Wu, X.; Pandey, T.; Jin, C.; Singh, A. K.; Akinwande, D.; Lin, J.-F. Pressure-Induced Semiconducting to Metallic Transition in Multilayered Molybdenum Disulphide. *Nature Communications* **2014**, *5* (1), 3731. https://doi.org/10.1038/ncomms4731.

(6) Kozawa, D.; Carvalho, A.; Verzhbitskiy, I.; Giustiniano, F.; Miyauchi, Y.; Mouri, S.; Castro Neto, A. H.; Matsuda, K.; Eda, G. Evidence for Fast Interlayer Energy Transfer in MoSe 2 /WS 2 Heterostructures. *Nano Letters* **2016**, *16* (7), 4087–4093. https://doi.org/10.1021/acs.nanolett.6b00801.

(7) Fu, Y.; He, D.; He, J.; Bian, A.; Zhang, L.; Liu, S.; Wang, Y.; Zhao, H. Effect of Dielectric Environment on Excitonic Dynamics in Monolayer WS2. *Advanced Materials Interfaces* **2019**, *6* (23), 1901307. https://doi.org/10.1002/ADMI.201901307.

(8) Eizagirre Barker, S.; Wang, S.; Godiksen, R. H.; Castellanos, G. W.; Berghuis, M.; Raziman, T. V; Curto, A. G.; Gómez Rivas, J.; Eizagirre Barker, S.; Gómez Rivas, J.; Wang, S.; Godiksen, R. H.; Castellanos, G. W.; Berghuis, M.; Curto, A. G. Preserving the Emission Lifetime and Efficiency of a Monolayer Semiconductor upon Transfer. *Advanced Optical Materials* **2019**, *7* (13), 1900351. https://doi.org/10.1002/ADOM.201900351.

(9) Liu, F.; Li, Q.; Zhu, X.-Y. Direct Determination of Momentum-Resolved Electron Transfer in the Photoexcited van Der Waals Heterobilayer WS2/MoS2. *Physical Review B* **2020**, *101* (20), 201405. https://doi.org/10.1103/PhysRevB.101.201405.